Journal of Materials Chemistry A

PAPER

View Article Online
View Journal

Cite this: DOI: 10.1039/c7ta10219d

Sustainable one-step strategy towards low temperature curable superparamagnetic composite based on smartly designed iron nanoparticles and cardanol benzoxazine†

Monisha Monisha, [a] Nisha Yadav, [a] Shashi B. Srivastava, [b] Samarendra P. Singh [b] and Bimlesh Lochab [*a]

Despite recent advances in polybenzoxazines (PBzs), especially of sustainable origin, the lowering of the curing temperature still remains a challenge in addressing their exploration in low-temperature processing applications. Innovative iron-based catalysts which are naturally abundant, cost-effective, and with larger surface area could demonstrate a practical, economic and facile approach for the development of iron NPs–polybenzoxazine composites. Here we propose an approach to develop a composite based on smartly-capped iron nanoparticles (NPs) and agro-waste phenolic-sourced cardanol benzoxazine monomer as a one-step solution with the benefits of lowering the curing temperature and providing superparamagnetism. NPs are smartly designed with a variation in the nature of the functionality in the capping agent and are characterized by thermogravimetry analysis (TGA), Fourier transform infrared (FTIR), powder X-ray diffraction (XRD), scanning electron microscopy (SEM), and transmission electron microscopy (TEM). The NPs showed a spherical shape of ~10 nm in size with appreciable magnetic characteristics. Both iron ions and available functionalities in the capping agent endow benefits in lowering the curing temperature of cardanol benzoxazine (64 °C), and enhancing its maximum thermal stability (34 °C), as determined by differential scanning calorimetry (DSC) and TGA, respectively. In addition, the nature of the chemical linkages in the polybenzoxazine network and the initial growth in the molecular weight of the polymer were found to be influenced by iron NPs, as supported by FTIR, nuclear magnetic resonance (^{1}H-NMR), UV-visible (UV-vis) spectroscopy, and gel permeation chromatography (GPC). The capping-agent-facilitated NPs distribution in the polybenzoxazine matrix was determined by atomic force microscopy (AFM). Polymer nanocomposites even with a 5 wt% loading of NPs showed good magnetic saturation and superparamagnetic behavior. The present work demonstrated a one-step solution with the incorporation of NPs in a benzoxazine monomer accounting for modification in the properties of polybenzoxazine composites with the benefits of magnetism.

Received 20th November 2017
Accepted 6th January 2018

DOI: 10.1039/c7ta10219d

rsc.li/materials-a

Introduction

Amongst conventional thermoset resins, such as phenol-formaldehyde, epoxy, and bismaleimides, polybenzoxazines (PBzs) are an upcoming class of resins with exceptional performance and versatility at a reasonable cost.[1] The superior and attractive properties of PBzs include near-zero volumetric shrinkage during curing, low water absorption, a high glass transition temperature (T_g) and char yield, excellent flame and chemical resistance, and high mechanical strength. PBzs also offer low surface energy, excellent dimensional stability with no release of toxic by-products during curing, a prolonged shelf life and ease of processability.[2] In addition, the flexibility of the synthetic design and ease of monomer synthesis in a one-step atom-economized manner further facilitate their viability at the industrial level. Moreover, there is further scope for benzoxazine advancement due to their unique reactive properties and compatibility with many other resins to produce hybrid formulations with excellent properties.[1]

An immense scope for the commercialization of PBzs is suggested by the rapid increase in expected global demand for phenolic resin to $16.05 billion by the year 2022.[3] One of the

[a]Materials Chemistry Laboratory, Department of Chemistry, School of Natural Sciences, Shiv Nadar University, Gautam Buddha Nagar, Uttar Pradesh 201314, India. E-mail: bimlesh.lochab@snu.edu.in; Fax: +91 120 30 01 580; Tel: +91 120 38 19 100 (Ext. 257)

[b]Department of Physics, School of Natural Sciences, Shiv Nadar University, Gautam Buddha Nagar, Uttar Pradesh 201314, India

† Electronic supplementary information (ESI) available. See DOI: 10.1039/c7ta10219d

major raw materials, widely consumed in high tonnages, for phenolic resin is bisphenol-A (BPA). However, BPA is relatively resistant to degradation and it is known to induce toxicity by acting as an endocrine disruptor. It is known that traces of BPA in resins affect populations of both humans and wildlife, and it is therefore banned or restricted in its use in several products.[4] This led to the imposition of stringent regulations by the European Phenolic Resins Association (EPRA), Registration, Evaluation, Authorization and Restriction of Chemicals (REACH), and the U.S. Environmental Protection Agency (EPA) on phenolic resin industries. In addition, disputes over carbon footprints and an escalation in petroleum prices may hamper the expansion of such industries to the next level. Despite numerous advantages of PBzs over traditional thermoset resins, their scope is currently limited due to their dependence on fossil reserves for phenol, and the requirement for a high curing temperature (~180–250 °C). Amongst naturally occurring phenols, cardanol appeared to be an attractive choice, being a renewable, non-toxic, agro-waste, of non-food origin, and it may exhibit natural degradation due to being a bio-source. It is extracted from cashew nut trees which are widely grown in tropical countries, mainly Brazil, India, and Vietnam. A high natural abundance with the simplest and inexpensive extraction methodology and a substantial annual industrial production (450 000 metric tonnes) is appealing for an exploration of its potential as a renewable chemical feedstock for polymers.[5,6] Furthermore, the low viscosity (145 mPa s at 43 °C) of cardanol is prudential for both solvent-free synthesis and processability to mitigate issues associated with volatile organic compounds (VOCs) to a great extent.[7,8] Its environmental compatibility due to its greener origin, and green processing with cost viability (US $2000–3000 per metric tonne) is attractive for reaping the benefits of cardanol at an industrial scale.

In general, the curing reaction of benzoxazine (Bz) monomers is initiated by thermally mediated ring-opening polymerization (ROP) which often demands a higher operating temperature (≥180 °C) which is adverse for both the processing and the fabrication of PBz composites. Generally, lowering the curing temperature is tackled by the external addition of catalysts. However, limited success has been achieved so far. Furthermore, the utility and entrapment of the catalyst may impose a high operational cost, safety concerns, and maintenance issues which may limit the widespread application of PBzs. Efforts to lower the curing temperature reported so far include either modification of the synthetic protocols to engineer the structure of the monomer at a molecular level or modification of the nature of the curing catalyst along with miniaturization from macro- to nano-level.[9] However, the former process being multi-step is affected by a plethora of conventional drawbacks: *viz.* energy-intensiveness, cost-intensiveness, lengthy solvent-based procedures, plus lower yields of benzoxazine monomer of the desired purity. While the latter solution also suffers from limitations caused by the deterioration of the properties of the cured resin due to entrapment of the catalyst which slowly leaches out over time, which has considerably plagued the arena of PBzs. Moreover, the added catalyst does not enhance any beneficial properties of the resin. Despite numerous efforts, neither the temperature nor the time required for curing Bzs are reduced substantially. In the synthetic approach, the curing reaction of the Bz monomer is facilitated at a moderate temperature by altering the structure of the monomer or by the addition of comonomers. This includes enhancement of the number of polymerizing oxazine functionalities, and the introduction of covalently-linked acidic functionalities in the monomer.[10–12] Recently copolymerization of Bz with elemental sulfur lowered the ROP with an extension of its utility in Li–S batteries.[13–15] The external addition of initiators to promote the ring-opening reaction of the oxazine ring in the monomer is commonly adopted due to its relative ease and the screening of several types of curing aids at a time. The initiators explored are phenols, acids, Lewis bases/acid, metal salts *etc.*[16,17] Metal-mediated Bz ROP reactions were demonstrated by Ishida *et al.* using metal halides and trifluoromethane sulfonates.[18] Amongst the complexes, transition metal acetylacetonate complexes of manganese, cobalt, and iron were found to be efficacious in exhibiting high catalytic activity without undermining the thermal stability of polybenzoxazines.[19] Previous work suggested that not only is the metal center controlling the catalytic activity of the initiators, but even the nature of the associated counter anion showed a profound role in the Bz ROP. A variety of lithium salts dictated the degree of monomer conversion along with a lowering of the curing temperature in PBzs.[20,21] The formation of oligomers was indicated at room temperature in 2 days using iron chloride as a catalyst.[22] Further polymerization reactions in Bz monomers are extended to metal–organic frameworks (MOFs) and nano-alumina particles, accounting for a lower curing temperature.[9,23] As compared to a bulk catalyst, the catalytic efficacy in MOFs and nanoparticles (NPs) primarily occurs due to the availability of an ultra-high surface area in the former, and both a higher surface area to volume ratio and nano-confinement effects in the latter.

Ideally, a catalyst-free ROP reaction is the preferred sustainable solution. If this is not feasible, the utility of a catalyst which is naturally abundant, cheap, and possesses low toxicity, could be a more practical, economic and facile approach for the polymerization of Bzs. In addition, the lowering of the curing temperature, and the opening up of a new arena of applications is of particular interest in our research group. Magnetic NPs and their polymer composites find applicability across the spectrum in varied fields, ranging from sensors, electromagnetic wave absorption, catalysis, and magnetic resonance imaging, to data storage.[24,25] The occurrence of a higher surface area in NPs, the scope for variation in the nature of capping agents and the availability of empty d-orbitals in iron ions are promising features in iron NPs, along with the benefits of magnetism. This motivated us to explore the incorporation of magnetic iron NPs as potential curing promoters with an extension of their applications in the magnetism domain that is also an attractive sustainable strategy in renewably sourced PBz.

Knowing the potential and effectiveness of bulk iron salts, and acidic carboxylic and basic amine group functionalities in assisting the ROP of benzoxazine, we designed and synthesized

iron magnetite NPs with and without a coated surface: namely $(Fe)_{TA}$, $(Fe)_{ATA}$, and $(Fe)_0$, respectively. The coating on iron NPs is based on aromatic acids, terephthalic acid (TA) and 2-aminoterephthalic acid (ATA), where the former contains two carboxylic acid groups and the latter contains additional amino groups along with two carboxylic acids. The carboxylic groups will stabilize the iron NPs while free unbound functionalities, carboxylic and/or amino groups, would facilitate the ROP of benzoxazine. The effect of the coating was studied by comparing the results with uncoated iron NPs, $(Fe)_0$. The NPs were characterized by powder X-ray diffraction (XRD), Fourier transform infrared (FTIR), scanning electron microscopy (SEM), and transmission electron microscopy (TEM). The effect of the incorporation of NPs in a cardanol-based benzoxazine monomer was studied by differential scanning calorimetry (DSC), thermogravimetry analysis (TGA), gel permeation chromatography (GPC), XRD and atomic force microscopy (AFM). A probable occurrence of linkages in the PBz network was supported by FTIR, nuclear magnetic resonance (^{1}H-NMR), and UV-visible (UV-vis) spectroscopy. Finally, PBz-iron nanoparticle composites were analyzed with a vibrating sample magnetometer (VSM) to determine their magnetic properties. Our work demonstrates that iron NPs serve a dual purpose, *viz.* a catalytic effect and the introduction of superparamagnetic behaviour in the cardanol polybenzoxazine resin, revealing a successful one-step sustainable strategy for the formation of a low-temperature curable superparamagnetic renewable phenol-based iron nanoparticles composite. This study provides new insights for the further development and design of an efficient nanomaterials catalyst for the formation of PBz polymers and their utility in specific applications.

Experimental

Materials

Cardanol (ρ = 0.9272–0.9350 g cm^{-3}; iodine value 250; acid value max 5; hydroxyl value 180–190) was procured from Satya Cashew Chemicals Pvt. Ltd. (India), paraformaldehyde from Fisher Scientific, hydrogen peroxide (30% w/v) and chloroform from Finar, anhydrous sodium sulfate from Chemlabs, sodium borohydride and *p*-rosaniline hydrochloride from CDH, ethanol from Emsure, ferric chloride ($FeCl_3 \cdot 6H_2O$), ferrous chloride ($FeCl_2 \cdot 4H_2O$), 2-aminoterephthalic acid (ATA), terephthalic acid (TA), ammonium hydroxide (NH_4OH, 28%), ascorbic acid, and *o*-phenanthroline were procured from Alfa Aesar. All reagents and solvents were used as received.

Methods

FTIR spectra were recorded on a Nicolet iS5 spectrometer equipped with an attenuated total reflectance diamond accessory (iD5-ATR) in the range of 4000–400 cm^{-1}. Absorbance measurements were carried out on a Thermo Scientific Evolution 201 UV-visible spectrophotometer for nanomaterials and monomer in deionized water and a mixture of tetrahydrofuran : water (2 : 1), respectively. Proton and carbon nuclear magnetic resonance (^{1}H- and ^{13}C-NMR) of the samples were recorded on a Bruker 400 MHz FTNMR spectrometer using deuterated chloroform ($CDCl_3$) as solvent and tetramethylsilane as an internal standard. The curing behavior of the monomers was evaluated by DSC (TA instruments). For dynamic DSC scans, samples (5 ± 2 mg) were enclosed in hermetic aluminium pans and heated from 30 to 350 °C at 10 °C min^{-1} under a nitrogen purge at a constant flow rate of 50 mL min^{-1}. Prior to the experiments, the instrument was calibrated for temperature and enthalpy using standard indium and zinc. Thermal equilibrium was regained within 1 min. of sample insertion, and the exothermic reaction was considered to be complete when the recorder signal levelled off to the baseline. The characteristic thermal parameters determined were T_i (initiation of polymerization), T_o (onset of polymerization is the intersection of the tangents of the peaks with the extrapolated baseline), T_p (peak temperature of the curing profile), and ΔH cure (the heat liberated during the curing reaction, *i.e.* the area under the curing profile) from the DSC curves. Thermogravimetric analysis (TGA) of aromatic acids, NPs, cured monomer and blends was performed with a PerkinElmer Diamond STG-DTA in the temperature range 30 to 800 °C and a heating rate of 10 °C min^{-1} under a nitrogen atmosphere at a flow rate of 50 mL min^{-1}. Number- and weight-average molecular weights (M_n and M_w) and polydispersity index (PDI = M_w/M_n) were estimated by GPC using a Viscotek Model 305 TDAmax with a refractive index detector. The GPC system was calibrated with polystyrene standards and data were analyzed using Omnisec software. Samples were dissolved in tetrahydrofuran solvent (3–4 mg mL^{-1}) and filtered through a 0.2 μm polytetrafluoroethylene filter before injection. XRD analysis was performed on a Bruker D8-Discover using Cu-K_α radiation (λ = 0.154 nm) to characterize the nature of the NPs and to determine their size. AFM (PARK, XE-007) in tapping mode, field emission scanning electron microscopy (FESEM, Carl Zeiss Ultra 55) and high-resolution transmission electron microscopy (HRTEM, JEOL-2100F) were used to determine the surface distribution of NPs in a polymer matrix, and the morphology of the NPs. The magnetic characterization was performed on a vibrating sample magnetometry (VSM) probe at an applied field of 1.5 tesla at room temperature from Cryogenic Ltd. Saturation magnetization (M_S) was obtained by the linear extrapolation of magnetization *vs.* the inverse of the magnetic field. Residual magnetism (M_R) is the magnetization left behind in a magnetic material after an external magnetic field has been removed: *i.e.* the magnetic flux density that remains in a material when the magnetizing force is zero.

Synthetic procedures

Synthesis of C-trisapm. Synthesis of benzoxazine monomer (C-trisapm) has been adapted from the literature.[26] To a solution of *p*-rosaniline hydrochloride (0.50 g, 1.54 mmol) prepared in ethanol (40 mL), sodium borohydride (0.53 g, 14.00 mmol) was added in two lots with continuous stirring in an ice bath. The reaction continued until a colour change from deep pink to yellow was noticed. Upon completion, the reaction was quenched with the addition of water (75 mL) to form a yellow

precipitate of amine, trisapm which was separated by simple filtration. Yield 84%. FTIR-ATR (diamond crystal/cm^{-1}): 3336, 3203, 3029, 1608, 1507, 1267, 815, 770; ^{1}H-NMR (400 MHz, $CDCl_3$, δ ppm): 6.88 (d, 6H, ArH), 6.59 (d, 6H, ArH), 5.24 (s, Ar_3CH), 3.56 (br, s, 6H, $-NH_2$); LC-MS (ESI interface-positive ions): $[M + H]^+$ 290.1651 (290.1613). A mixture of cardanol (1.56 g, 5.18 mmol), paraformaldehyde (0.31 g, 10.36 mmol) and trisapm (0.50 g, 1.72 mmol) was heated at a temperature of 90 °C for 5 h. C-trisapm was obtained as a viscous brown oil. Yield 80%; FTIR-ATR (diamond crystal/cm^{-1}): 3007, 2923, 2852, 1657, 1615, 1508, 1255, 1198, 1109, 1040, 990, and 960; ^{1}H-NMR (400 MHz, $CDCl_3$, δ ppm): 0.89 (CH_3, t), 1.30 [$(CH_2)_n$, m], 1.57, 2.02 (CH_2CH═, m), 2.50 (CH_2Ar, *t*), 2.78 [$CH_2(CH$═$)_2$, m], 4.55 (s, $ArCH_2N$–), 5.26–5.35 (m, CH═, CH_2═CH–, $-OCH_2N$–, HC═CH_2, Ar_3CH); ^{13}C-NMR (100 MHz, $CDCl_3$, ppm): 50.32 ($ArCH_2N$–), 54.5 (Ar_3CH), 79.52 ($-OCH_2N$–); LC-MS (ESI interface-positive ions) [C-trisapm]$^+$: 1268.8966, 1267.8904, 1266.8904 1265.8816, 1264.8783, 1263.8689, 1262.8649, 1261.8551 (monoene: 1267.9408, diene: 1261.8938, triene: 1255.8469).

Synthesis of nanoparticles $(Fe)_0$, $(Fe)_{TA}$, and $(Fe)_{ATA}$. Iron nanoparticles were synthesized using the chemical co-precipitation method, according to the reported procedure.[27] In brief, $FeCl_3 \cdot 6H_2O$ (2.8 g, 10.35 mmol) and $FeCl_2 \cdot 4H_2O$ (1.0 g, 5.02 mmol) were dissolved in deionized water (50 mL) in 2.06 : 1 molar ratio. The so-formed yellow solution was stirred (~400 rpm) with heating at 80 °C for 1 h under a continuous flow of nitrogen atmosphere to minimize air oxidation of Fe(II) ions. To this, aqueous ammonium hydroxide (23% w/v, 6 mL) was added rapidly to attain a pH of 10–11. During addition of ammonium hydroxide, the reaction mixture became viscous; therefore the stirring speed was increased to ~1000 rpm to ensure homogenization. The resultant suspension was stirred vigorously for another 1 h at 80 °C and then allowed to cool to room temperature. The obtained suspension was filtered and washed with an ethanol : water mixture (3 : 1, 45 mL × 2). The solvent was removed under a rotary evaporator in vacuum at 50 °C to yield uncoated iron nanoparticles $(Fe)_0$ as a black powder (2.5 g).

Similarly, TA- or ATA-coated iron nanoparticles, namely $(Fe)_{TA}$ or $(Fe)_{ATA}$, were synthesized by adding 1.9 g of terephthalic acid (TA) or 2-aminoterephthalic acid (ATA) along with $FeCl_3 \cdot 6H_2O$ (2.8 g) and $FeCl_2 \cdot 4H_2O$ (1.0 g) in the above procedure, respectively. The coated NPs, $(Fe)_{TA}$ and $(Fe)_{ATA}$ were obtained as dark brown powders with yields of 2.5 g and 2.9 g, respectively.

Preparation of blends. The suspension of each type of nanoparticle (5 wt%) in chloroform (5 mL) was bath sonicated for 1 min. before its addition to a rapidly stirred viscous oil of C-trisapm. The blend was stirred for 10 min. before being kept in a vacuum oven at 40 °C for 1 h. The mixture was homogenized at regular intervals of 10 min. to remove any trapped solvent. The so-obtained resultant blends are abbreviated as C-trisapm$(Fe)_0$, C-trisapm$(Fe)_{TA}$ and C-trisapm$(Fe)_{ATA}$, according to the nature of added NPs: *i.e.* $(Fe)_0$, $(Fe)_{TA}$, or $(Fe)_{ATA}$, respectively.

Thermal polymerization of monomer and blends. 50 mg of neat monomer or its blend with iron NPs (5 wt%) was placed in each of a set of 10 test-tubes and kept in a preheated oil bath at 150 °C under a nitrogen atmosphere. The test tubes were taken out from the oil bath one-by-one at intervals of 30 min. over a period of 8 h. The withdrawn test tubes were allowed to cool to room temperature before any analysis. The contents of the test tubes were dissolved in the desired solvent (deuterated *vs.* non-deuterated) and pre-filtered followed by analysis by ^{1}H-NMR, UV-vis and GPC. The former techniques were used to determine any structural and absorption change in the monomer while latter is used to estimate M_n and M_w to determine the growth in molecular weight of the monomer, if any. In order to assist the solubility of the formed polymer, the mixture was kept in the solvent overnight at room temperature before recording any analysis.

Quantitative estimation of released Fe(II) ions by nanoparticles. Iron NPs (50 μg, 1 mL) were reduced by ascorbic acid (10 mM, 1 mL) and then reacted with *o*-phenanthroline (0.1%, 1 mL) at room temperature. The reaction mixture was diluted with distilled water to keep a total volume of 5 mL. The complexation reaction was monitored by recording the UV-vis spectra of the so-formed red-colored complex at different time intervals.[28] The observed absorbance intensity of the complex at λ_{max} 512 nm was correlated with the concentration of iron ions, using the standard curve of $FeCl_3$ ($y = 0.00479x + 0.05797$, $R^2 = 97.03\%$).

Oxidative polymerization of C-trisapm monomer. The oxidative polymerization of C-trisapm was performed using $(Fe)_0$ and hydrogen peroxide as a catalyst and an oxidizing agent, respectively, at room temperature under an air atmosphere. In a vial, $(Fe)_0$ (1 mg mL^{-1}, THF, 5 wt%) was bath-sonicated for 30 s before adding a solution of C-trisapm (19 mg mL^{-1}, THF) and hydrogen peroxide solution (30% w/v, 40 μL in 1 mL of distilled water). The time of addition of the monomer was taken as $t = 0$ for the reaction. The progress of the reaction was monitored by recording the UV-vis spectra of aliquots (50 μL) withdrawn from the reaction mixture in distilled water (3 mL).

Results and discussion

Benzoxazine monomer synthesis requires three reagents, namely phenol, amine and formalin, which condense mainly in presence of solvent. On account of its sustainability, the utility of its agro-waste origin and its reactive diluent properties, cardanol is an ideal phenolic feedstock for the solventless preparation of the Bz monomer. Cardanol is derived from the thermal treatment of cashew nut shell liquid, which in turn is processed from the outer mesocarp of the cashew fruit (*Anacardium occidentale* L.). The amine (trisapm) component of the benzoxazine is chemically reduced *p*-rosaniline hydrochloride, which is a widely-explored organic dye at the industrial level. The presence of three primary amine functional groups in trisapm is beneficial to forming three oxazine rings in the Bz monomer. The monomer was synthesized by Mannich-like condensation reaction of trisapm and cardanol, adapting the solventless, one-pot methodology to form C-trisapm in quantitative yields (Fig. S1†). The ^{1}H-NMR (Fig. S2a†) of C-trisapm suggests its successful synthesis and the formation of an oxazine ring is

indicated by signals at 4.55 ppm (labelled as "a") and in the region 5.35–5.26 ppm (labelled as "b") due to the formation of $ArCH_2N$– and –OCH_2N– linkages. ^{13}C-NMR (inset, Fig. S2a†) further confirms its formation due to the appearance of characteristic signals at ~50.3 ppm and ~79.5 ppm due to $ArCH_2N$ and $ArOCH_2N$, respectively. The FTIR spectrum (Fig. S2b†) of C-trisapm showed the characteristic C–O–C asymmetric and symmetric stretches at 1255 cm^{-1} and 1040 cm^{-1}, suggesting condensation of the phenolic –OH of cardanol and the –NH_2 group of trisapm. The existence of a higher number (three) of reactive oxazine functionalities in C-trisapm accounts for its benefits of a faster curing potential and high conversion rates amongst its cardanol-derived contemporaries.[26] The utility of cardanol benzoxazines may still be affected by their higher ROP temperature, and efforts to mitigate the requirements for a higher curing temperature can be tackled with smart solutions. So far, curing promoters, in general, aided in lowering the curing temperature in Bzs, which remain trapped within the cured PBz matrix, damaging the properties of the polymer over time. Recent evolution and advances in the utilities of polymers demand a one-step solution: *i.e.* besides lowering the curing temperature, an additional benefit in a property or application will be advantageous in minimizing extra processing steps. For this reason, iron NPs are a versatile choice and are expected to lower the curing temperature and impart magnetic properties to a sustainable cardanol-based PBz matrix.

Amongst available NPs synthetic methods, chemical preparation *via* co-precipitation is the most commonly adopted strategy due to its simple, amenable, cost-effective, and efficient protocol. The process allows an ease of control of reaction parameters to vary the composition and shape of NPs.[29] Iron oxide NPs were synthesized by base-mediated co-precipitation of aqueous solutions of Fe^{2+} and Fe^{3+} ions (Fig. 1).

The chemical oxidation of NPs can be averted by surface modification and capping agents to provide the benefits of stability, ease of dispersion in solvents, compatibility with the organic matrix to mediate their processing and further functionalization. Previous reports on Bz polymerization suggested –COOH and –NH_2 groups as potential catalysts to assist ROP, and in addition, both groups are polar in nature, which may assist their dispersion in the monomer *via* dipolar interactions.

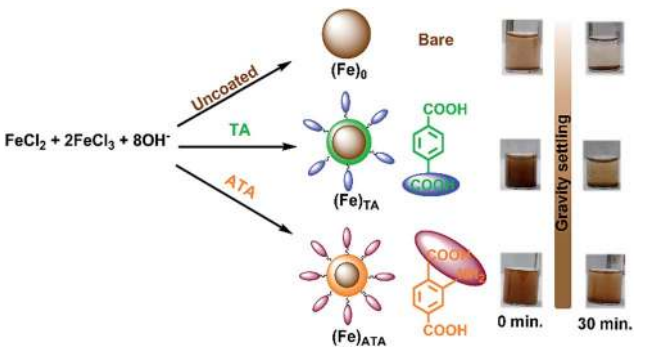

Fig. 1 Generalized synthetic scheme of three types of synthesized iron NPs, with digital images of their aqueous suspension (2.5 mg mL^{-1}).

Therefore synthesized NPs were capped with organic aromatic acids, terephthalic acid (TA) and aminoterephthalic acid (ATA), possessing carboxylic acid groups to undergo a covalent reaction at the surface of magnetite to form $(Fe)_{TA}$ and $(Fe)_{ATA}$. In addition, bare NPs were also synthesized without a coating on their surface, $(Fe)_0$, to study both the role of coating and the availability of a reactive iron surface in benzoxazine polymerization. In general, the absence of organic functionalities in unmodified NPs is well known to drastically affect the properties of polymer nanocomposites due to their aggregation. The stability of the suspension of synthesized iron NPs is evident from the digital images (Fig. 1). $(Fe)_0$ nanoparticles almost settled within 30 min., followed by $(Fe)_{TA}$, then $(Fe)_{ATA}$. This gravity settling can be explained on the basis of the absence of any stabilizing hydrophilic coating in the former, while the surfaces of the latter NPs possess a polar carboxylic or/and an amine functionality which can extend polar interactions with both C-trisapm monomer and processing solvents.

The existence of a coating, the nature of the functionalities, and the molecular composition of the NPs were confirmed by FTIR spectra (Fig. 2a). The appearance of a peak at 585 cm^{-1} is apparent in all the synthesized NPs and is related to the Fe–O stretch.[30] The presence of a broad band at 3200–3600 cm^{-1} indicated the presence of surface hydroxyl groups on iron, bound water, and N–H due to amine groups (in the case of ATA-coated NPs). The O–H stretch due to carboxylic groups appeared in the region 2500–3000 cm^{-1}. The lower intensity, broadness and the absence of certain peaks in the 2500–3600 cm^{-1} range are evident in the case of $(Fe)_0$ NPs. The presence of a capping on $(Fe)_{TA}$ and $(Fe)_{ATA}$ was suggested by the aromatic C–H stretch of TA and ATA centered at 3132 and 3023 cm^{-1}. The carboxylic group of the capping agents, *i.e.* TA and ATA, can be bound to the Fe ions in NPs either through the two O atoms of a carboxylate ion and/or by one O atom alone to form Fe–O–C linkages. The existence of a carboxylate ion is indicated by the presence of symmetric and asymmetric stretches due to C–O centered in the regions of ~1408 cm^{-1} and ~1552 cm^{-1}, respectively. The

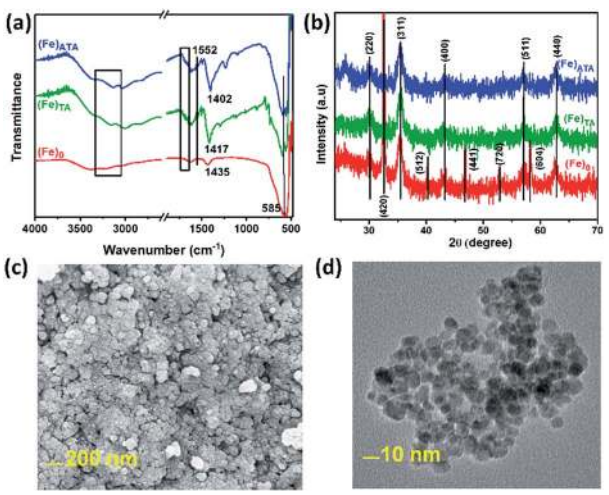

Fig. 2 Characterization of iron NPs: stacked (a) FTIR and (b) XRD spectra; (c) SEM and (d) TEM images of $(Fe)_{ATA}$ NPs.

unbound and free carboxylic acid groups are evident in the region centered around 1680 cm^{-1} due to the C=O stretch of the carboxylic group. In addition, O–H bending vibrations due to water molecules around the NPs also appeared in the region 1600–1700 cm^{-1}.[31] The existence and prominent nature of IR peaks due to the surface functionality in $(Fe)_{TA}$ and $(Fe)_{ATA}$ suggested the presence of a coating on their surfaces.

The structural phase composition of iron NPs was studied using XRD (Fig. 2b). The peaks of synthesized iron NPs matched well with the magnetite (Fe_3O_4) NPs PDF data [JCPDS no. 01-086-1343]. In the case of $(Fe)_0$ a very intense peak at 32.56 (420) plane [JCPDS no. #00-016-0653] along with the corresponding XRD peaks confirm the co-existence of maghemite (Fe_2O_3) structures. The co-formation of maghemite with magnetite is attributed to the aerial oxidation of Fe^{2+} ions to form Fe^{3+} ions due to the high surface activity of their uncoated surface.[32] It is worth mentioning that, even though all the NPs are synthesized with the same feed ratio of Fe^{3+}/Fe^{2+}, the corrosion in $(Fe)_0$ NPs explains the change in its chemical composition, accounting for a higher content of Fe^{3+} at the expense of Fe^{2+}. This accounts for the change in the composition of $(Fe)_0$ NPs, which contain a relatively higher concentration of Fe^{3+} ions compared to $(Fe)_{TA}$ and $(Fe)_{ATA}$. The formation of maghemite can be relatively avoided by capping agents in NPs, which is evident from the absence of a peak at $2\theta = 32.56°$ in $(Fe)_{TA}$ and $(Fe)_{ATA}$. XRD peaks are broad, suggesting the smaller crystallite size of the Fe_3O_4 particles. The average crystallite size of different NPs was calculated from the Debye–Scherrer equation using the peak at 311 at $2\theta = 35.48°$. The size varies from 9.4, 9.1 to 8.4 nm for $(Fe)_0$, $(Fe)_{TA}$ and $(Fe)_{ATA}$, respectively, suggesting the role played by the capping agent in stabilizing the smaller size.

Fig. 2c and d show the SEM and TEM images of the representative iron NPs. From the images, it can be seen that the NPs are spherical in shape with a narrow particle size distribution, suggesting a nearly monodispersed system. A mean diameter of ~10 nm is observed, which corroborates the XRD results well.

The amount of coating on the surface of the NPs was determined by thermogravimetry analysis (TGA), Fig. 3c. A mass loss of only 5% was obtained in uncoated $(Fe)_0$ NPs when heated from 50 to 800 °C, which is attributed to the removal of physico- and chemi-adsorbed water molecules. However, coated NPs showed a small mass loss in the 100–200 °C range which is due to the loss of physico-sorbed water, hydrogen bonded due to the polar nature of the NP surface. The total% mass loss follows the order $(Fe)_0 < (Fe)_{TA} < (Fe)_{ATA}$. The char yield ($Y_c$) at 800 °C of $(Fe)_{TA}$ and $(Fe)_{ATA}$ was found to be 79 and 73%, suggesting the amounts of capping agent as 16 and 22%, respectively. A higher percentage of organic coating in $(Fe)_{ATA}$ along with a higher number of surface functionalities [amine and carboxylic groups as compared to only a carboxylic group in $(Fe)_{TA}$] also accounts for the higher hydrophilicity and stability of the aqueous dispersion, which is in good agreement with the digital images in Fig. 1.

Blends of cardanol benzoxazine with NPs

Blends of C-trisapm loaded with the various types of synthesized nanoparticles, $(Fe)_0$, $(Fe)_{TA}$, and $(Fe)_{ATA}$, were prepared.

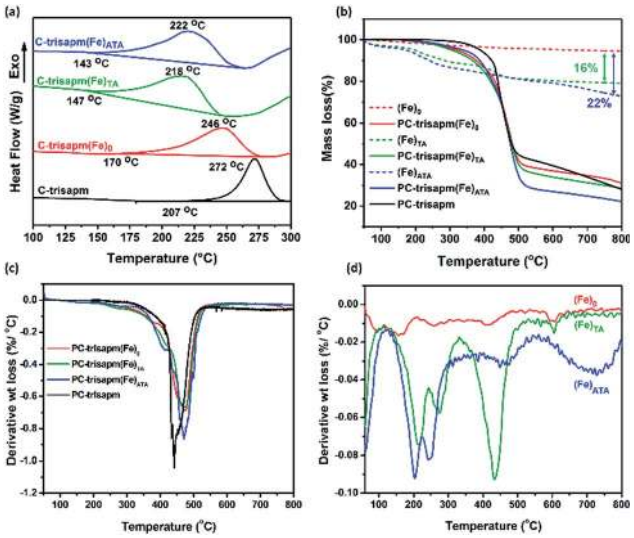

Fig. 3 Thermal characterization of NPs, monomer and their blends (a) DSC of blends; (b) TGA of cured polymer nanocomposites; DTG curves of (c) cured polymer nanocomposites, and (d) NPs.

Cardanol benzoxazine was found to be insoluble in organic solvents, such as methanol, ethanol, water, acetonitrile, or DMSO, but soluble in tetrahydrofuran and chloroform. Moreover, the dark color of the cardanol benzoxazine solution was found to obscure the visualization of the NPs. This affected the determination of their dispersion stability in the monomer solution. Therefore, digital images of both iron NPs and their blend with cardanol benzoxazine in chloroform and tetrahydrofuran are recorded (Fig. S3†). Interestingly, iron NPs showed a good dispersion in polar organic solvents, such as chloroform and tetrahydrofuran. It is reported that the stability of a dispersion of NPs is dictated by the nature of the coating, nanoparticle size, composition, and solvents. The choice of solvent further depends upon its polarity (extent of hydrogen bonding), surface tension and viscosity,[33,34] which influence the stabilizing forces of interactions. The lower viscosity (tetrahydrofuran 0.46 *vs.* chloroform 0.54 mPa s at 25 °C)[35] and tetrahydrofuran's ability to form a relatively higher H-bonding network than chloroform are found to be responsible for stabilizing the dispersion of synthesized iron NPs. All the synthesized NPs showed a respectable stability of dispersion, which is higher in tetrahydrofuran than in chloroform.

The properties of blends and so-formed polymers PC-trisapm$(Fe)_0$, PC-trisapm$(Fe)_{TA}$, and PC-trisapm$(Fe)_{ATA}$ were compared with each other and with respect to pristine monomer and PBz polymer. A smaller loading of NPs, *i.e.* 5 wt%, is chosen to study their catalytic role in the Bz ROP reaction, if any.

The curing behaviour of all blends and of neat monomer was studied by DSC (Fig. 3a) and the results are summarized in Table 1. The curing temperature of as-synthesized C-trisapm benzoxazine monomer showed a T_i of 207 °C. The addition of $(Fe)_0$ NPs in C-trisapm decreased T_i to 170 °C, which is attributed to the catalyzing effect of iron *via* co-ordination with the oxazine ring, thereby facilitating the ring-opening reaction.[22]

Table 1 Thermal characterization of NPs and blends

Sample	T_i (°C)	T_o (°C)	T_p (°C)	ΔH (J g^{-1})	Decrease in T_i (°C)	Decrease in T_p (°C)	Decrease in ΔH (J g^{-1})	$T_{5\%}$ (°C)	$T_{10\%}$ (°C)	T_{max} (°C)	Y_c at 800 °C (%)
C-Trisapm	207	254	272	108	—	—	—	387	421	442	28
C-Trisapm(Fe)$_0$	170	206	246	71	37	48	37	320	376	476	31
C-Trisapm(Fe)$_{TA}$	147	172	218	83	60	54	25	306	365	471	29
C-Trisapm(Fe)$_{ATA}$	143	190	222	89	64	50	19	340	386	470	22
(Fe)$_0$	—	—	—	—	—	—	—	655	—	—	95
(Fe)$_{TA}$	—	—	—	—	—	—	—	198	282	214; 274; 432	79
(Fe)$_{ATA}$	—	—	—	—	—	—	—	173	240	203; 246; 463; 722	73
TA	—	—	—	—	—	—	—	293	309	353	0
ATA	—	—	—	—	—	—	—	278	289	310	0

The addition of (Fe)$_{TA}$ and (Fe)$_{ATA}$ in C-trisapm to form C-trisapm(Fe)$_{TA}$ and C-trisapm(Fe)$_{ATA}$ further shifted T_i to a lower temperature of 147 °C and 143 °C, respectively, indicating the enhancement in catalytic efficiency of NPs due to the capping agent. Previous reports suggested that the incorporation of carboxylic group functionality in the structure of benzoxazine monomer is an effective design strategy to reduce the temperature of the ROP in the Bz monomer. The presence of such a carboxylic group is found to catalyze the ring opening *via* a cationic mechanism with a considerable lowering in curing temperature and simultaneously accounts for an *in situ* enhancement in crosslink density of the PBz network.[12,36] In contrast, exploration of the benzoxazine monomer with inherent carboxylic acid functionality as a stabilizing layer for Fe_3O_4 nanoparticles accounted for an increase in curing temperature from 166 °C to 190 °C.[37] This can be explained by the fact that the monomeric carboxylic groups might be involved in the stabilization and coating of nanoparticles and, hence, are unavailable for catalyzing the polymerization reaction. In our case, aromatic acids used to coat iron NPs, *i.e.* (Fe)$_{TA}$ and (Fe)$_{ATA}$, possess two carboxylic functionalities, where one –COOH is expected to stabilize the NPs and the other is exposed at the periphery and is available to catalyze the ROP of C-trisapm. Furthermore, structurally (Fe)$_{ATA}$ possess an additional surface amine functionality on its surface along with carboxylic groups which accounted for the greatest lowering in curing temperature, consistent with the literature.[38] Understanding the catalytic effect of NPs in the ring-opening reaction of the oxazine ring in C-trisapm is guided by the availability of three species, namely iron ions, –COOH and –NH_2 groups, and their abundance follows the order (Fe)$_0$ < (Fe)$_{TA}$ < (Fe)$_{ATA}$, which correlates well with the lowering of curing temperatures by 37, 60 and 64 °C, respectively. A reverse trend is observed in the heat of curing reaction (ΔH) values and is lowered by 37, 25, and 19 J g^{-1}, which is attributed to the unreactive content of NPs. This variation in ΔH may be accounted for by the amount and nature of capping agent in the NPs. Bare (Fe)$_0$ NPs showed a maximum lowering in ΔH value due to the absence of capping agent.

TGA thermograms of NPs, neat polymer and their polymeric blends were recorded (Fig. 3b and Table 1) to explore the effect of incorporation of NPs on the thermal stability of polymers. PC-trisapm showed a mass loss of 10% ($T_{10\%}$) at 421 °C while incorporation of NPs reduces it to lower temperatures. This could be accounted for by the existence of thermally labile linkages, functionalities such as capping agents and pendant groups which are not part of the crosslinked network. The TGA of aromatic acids (TA and ATA) was also recorded, to analyze the effect of the nature of the coating on the NPs on the thermal stability of the polymers. TGA and DTG traces (Fig. S4† and Table 1) revealed a higher decomposition temperature for TA than for ATA. The maximum decomposition temperatures (T_{max}) observed for TA and ATA were found to be 353 °C and 310 °C, respectively. A higher thermal stability of terephthalic acid than 2-aminoterephthalic acid could be attributed to the presence of a higher number of labile functionalities in ATA *vs.* TA (3 *vs.* 2). Interestingly, PBz resin cured with (Fe)$_{TA}$ and (Fe)$_{ATA}$ showed the reverse behaviour: *i.e.* a higher temperature for 5% ($T_{5\%}$) and 10% ($T_{10\%}$) mass loss was observed with (Fe)$_{ATA}$-cured monomer than with (Fe)$_{TA}$. This suggests the involvement of both amino and carboxylic functionalities in extending the formation of a dense polymer network, which is in accordance with the literature.[39] In cured resins, the T_{max} is shifted to the higher temperature upon incorporation of NPs, suggesting the formation of a different and more stable crosslinked network structure with varied and thermally stable linkages in the developed polymer (Fig. 3c). In general, PBz led to the formation of phenolic structures linked by Mannich bridges due to the thermally assisted ROP of oxazine rings. The T_{max} in PC-trisapm is in accordance with the literature, suggesting the predominance of phenolic Mannich bridges.[26] The existence of arylamine Mannich linkages,[40] *N*,*O*-acetal linkages[18] and the formation of carbonyl structures[41] are also reported to affect thermal stability. It is well known that *N*,*O*-acetal linkages tend to undergo a thermal rearrangement reaction to form more thermally stable linkages and such reactions are further facilitated by the presence of iron salts.[22] The formation of *N*,*O*-acetal linkages is favored in sterically hindered and ortho-blocked phenolic compounds.[42,43] It is probable that iron being a d-block transition metal may account for the formation of a network *via* bonding to heteroatoms O/N in the monomer and the polymer and may account for interconversion/formation of

a more thermally stable network and with a shift in maximum weight loss temperature to a higher temperature. In PBzs, the evolution of amines preceded phenol and formerly occurs at a lower temperature <400 °C.[44] A relatively higher amount of aniline is liberated during pyrolysis of thermally cured polyBA-a and a substantial reduction in release of aniline is observed when BA-a monomer is cured with $FeCl_3$ catalyst.[22] Similarly, we may also expect lower amine loss in the thermal degradation of iron NPs cured PBz resin. The analysis of thermally degraded products has not been performed currently and demands a further systematic study, which we may pursue in the near future. The smaller% mass losses at lower temperature can be understood from DTG traces of the cured resins and NPs (Fig. 3c and d). The lower temperature mass losses may be attributed to the liberation of the coating on the NPs from the polymer matrix, as observed from the inset of Fig. 3d. The char yield of neat polymer, *i.e.* PC-trisapm, is increased by curing with $(Fe)_0$ NPs, but it is lower in the presence of coated NPs, *i.e.* $(Fe)_{TA}$ and $(Fe)_{ATA}$. The char yield was found to be lowest in the case of $(Fe)_{ATA}$-cured PBz resin, PC-trisapm$(Fe)_{ATA}$, which can be correlated with a higher amount of coating on its surface.

Polymer blends were cured and studied by XRD to understand the incorporation of NPs and their crystalline structure in the polymer matrix. XRD peaks corresponding to Fe_3O_4 NPs were inconspicuous, which is due to their relatively lower loading (5 wt%) in the polymer matrix (Fig. 4a and b). In addition, a broad hump of the polymer at $2\theta = 20.09°$ is observed due to the formation of amorphous PC-trisapm domains by the ROP reaction. The size of the NPs in the PBz matrix was evaluated and a meagre increase in their crystallite size of 0.5–2 nm in the polymer matrix was observed, suggesting negligible aggregation and effective compatibilization of NPs in the cured resin. Surprisingly, a minimal change in size of bare $(Fe)_0$ NPs is observed, suggesting that C-trisapm may also assist in the stabilization of NPs *via* co-ordination through O or N atoms of oxazine functionality in a similar manner to externally organic acid coated NPs.

The surface of cured resins with different iron NPs, namely PC-trisapm$(Fe)_0$, PC-trisapm$(Fe)_{TA}$, and PC-trisapm$(Fe)_{ATA}$, was characterized using AFM to clarify the features of nanoparticles at the blend surfaces. This technique provides the surface topography of the grains formed due to the agglomerated nanoparticles. The 2D and 3D surface topography images for the polymer composites are shown in Fig. 4c. A uniform distribution of $(Fe)_{ATA}$ nanoparticles in the monomer was observed in comparison to $(Fe)_0$ and $(Fe)_{TA}$ NPs, which can be explained by the coated and uncoated surfaces. Moreover, a lower tendency for agglomeration in $(Fe)_{ATA}$ is accounted for by the higher amount of coating and the highly polar nature of the surface functionality. The grain size of $(Fe)_0$ and $(Fe)_{TA}$, and $(Fe)_{ATA}$ NPs in the PBz matrix was found to be in the range of 20–300 nm, 25–400 nm, and 20–300 nm, respectively (Fig. S5†).

Mechanistic aspect studied by FTIR, UV-vis, NMR and GPC

The mechanism of polymerization and the nature of the linkages in the NPs-catalyzed ROP of C-trisapm were studied by FTIR, UV-vis, NMR and GPC.

Isothermal FTIR analysis of cured C-trisapm in the presence/absence of NPs was recorded at 150 °C after 2 h (Fig. 5a). The methyl group of the alkylene chain in cardanol at 2922 cm^{-1} was selected as an internal standard and all the spectra were normalized at this wavenumber to assist the comparison. The characteristic absorption bands in C-trisapm due to C–O–C in the oxazine ring is observed at 1255 cm^{-1} (intense, asymmetric

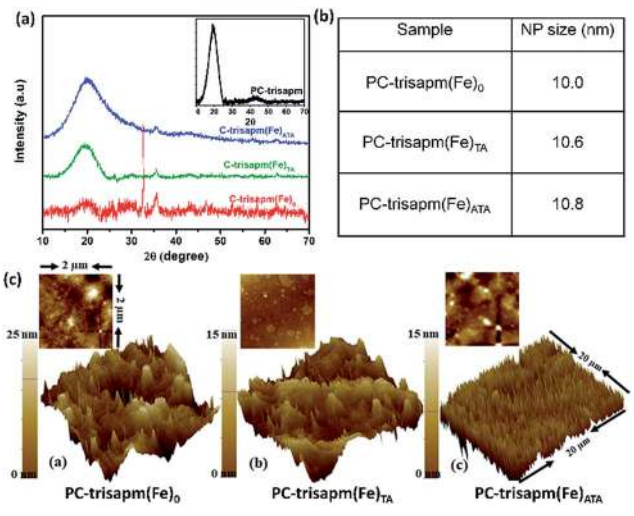

Fig. 4 (a) XRD pattern (inset shows XRD of neat PC-trisapm) and (b) crystallite size of nanoparticles in cured PBz resins; (c) 3D images of surface topography of cured polymer resins for 20 μm^2 scan area (inset shows 2D images of 2 μm^2 area, surface features with different grains sizes of NPs in the polymer matrix).

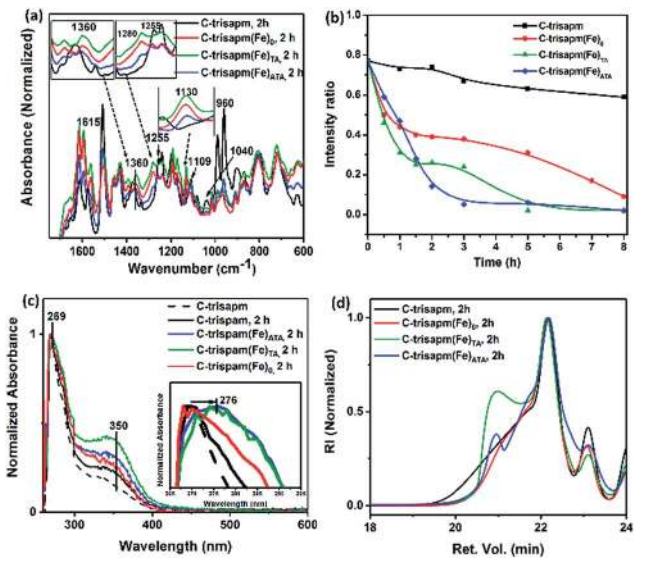

Fig. 5 Characterization of blends, C-trisapm after heating at 150 °C for 2 h (a) normalized transmission FTIR absorption spectra; (b) change in the intensity ratio of the $ArCH_2N$ peak with respect to the methyl peak of the alkylene chain in the cardanol ring; (c) normalized UV-vis spectra of leached out low molecular weight species in cured resin in DMSO as solvent (inset shows UV-vis spectra at 5 h); (d) normalized GPC chromatograms at room temperature.

stretch) and 1040 cm^{-1} (weak, symmetric stretch), respectively. During ROP, the oxazine ring opens up to form a polymer network, which is reflected as a decrease in intensity at these two bands, allowing them to be the most easily and widely monitored stretching frequencies in the Bz polymerization reaction. The FTIR spectrum of C-trisapm monomer upon thermal treatment (at 150 °C) showed no characteristic change within 2 h, which is attributed to its much higher ROP temperature, as determined by DSC. The presence of iron NPs in the monomer accounted for a substantial change in the FTIR spectrum of C-trisapm at 150 °C, which is consistent with the DSC results. Compared to as-synthesized C-trisapm, its blend with NPs showed a significant broadening of the peak at 1255 cm^{-1}, while the peak at 1040 cm^{-1} had nearly disappeared in 2 h. The enhancement in curing time to 5 h shows no significant decrease in the intensity of the peak at 1255 cm^{-1} (Fig. S6†). This suggests the pronounced effect of iron NPs on C–O–C stretching frequencies only within the first 2 h of heating. Simultaneously, the peaks centered at 1109 cm^{-1} and 960 cm^{-1} due to the C–N–C stretch and out-of-plane bending vibrations of the oxazine ring[45] were significantly reduced in intensity. The percentage change in C–O–C and C–N–C stretches with the addition of iron NPs is shown in Fig. S7.† Furthermore, the development of new peaks at 1130 and 1280 cm^{-1} was observed, while no such alterations were observed in the case of neat C-trisapm during the same time duration (inset in Fig. 5a). These new peaks are attributed to C–O–C and C–N–C stretches due to the coordination of hetero-atoms with the Fe^{3+}/Fe^{2+} ions present in NPs *via* Lewis acid–base interaction, which is consistent with the literature.[46] It is worth mentioning that the amount of iron loading is only 5 wt% w.r.t. monomer in the present system. Therefore, it can be visualized that not all C–O–C and C–N–C functionalities present in the ring-opened PBz will be linked to iron NPs. It may consist of coordinated and uncoordinated C–O–C and C–N–C bonds to the iron NPs. Such coordination acts as crosslinks which can be extended both inter- and intra-molecularly in a random manner to enable a chelating effect. A shift in C–O–C and C–N–C stretches towards higher energy is apparent as an increase in bond order due to co-ordinatively linked hetero-atoms with an enhancement in rigidity.[47] In addition to other linkages, these coordinative linkages may also be responsible for a higher thermal stability (T_{max}) in iron-containing PC-trisapm. In general, linkages formed across the PBz network due to the ring-opening reaction of the oxazine ring leads to a higher amount of substitution at the benzene ring of cardanol in the C-trisapm monomer. The probable linkages include phenolic Mannich, arylamine Mannich, and *N*,*O*-acetal type with tetra-, tri/tetra-, and tri-substituted benzene ring in PC-trisapm, respectively.

The peaks at 1615 cm^{-1} and 1360 cm^{-1} are attributed to the formation of tri- and tetra-substituted benzene rings respectively.[48] Upon heating, a significant increase in the intensity of 1615 cm^{-1} and a new peak at 1360 cm^{-1} (inset to Fig. 5a) developed with relatively much smaller intensity changes in iron NPs monomer blends. There is no peak corresponding to a tetra-substituted benzene ring in iron-free C-trisapm cured for the same duration, *i.e.* 2 h, suggesting no ROP in neat C-trisapm. In the iron monomer blends, a significant percentage increase in the intensity of 1615 cm^{-1} but a relatively a meagre change in intensity at 1360 cm^{-1} are observed (Fig. S8†), suggesting the predominance of tri-substituted benzene ring linkages in the polymer. To study whether the 1360 cm^{-1} stretch develops in as-synthesized C-trisapm, the curing time was prolonged to 8 h. Surprisingly, initially a peak at 1371 cm^{-1} is observed, which shifted to 1367 cm^{-1} then to 1360 cm^{-1} when heated for 2, 5 and 8 h, respectively (Fig. S9†). A further increase in time led to an enhancement in the peak intensity at 1360 cm^{-1} with no relative shift in wavenumber. However, in the presence of iron-cured samples, the 1360 cm^{-1} peak only developed within 2 h (inset of Fig. 4a), which is probably due to the formation of the tetra-substituted benzene ring in Bz monomer polymerization and is attributed to the occurrence of phenolic-Mannich and arylamine linkages. Moreover, tetra-substitution at the benzene ring can be envisaged if the monomer is susceptible to oxidative polymerization in the presence of iron, forming biphenyl linkages in the polymer. The percentage change in the intensity of both tri- and tetra-substituted benzene ring FTIR stretch follows the order C-trisapm < C-trisapm$(Fe)_{ATA}$ < C-trisapm$(Fe)_0$ < C-trisapm$(Fe)_{TA}$ (Fig. S8†). The predominance of *N*,*O*-acetal linkages over traditional phenolic Mannich structures is indicated in NPs-mediated polymerization.

The progress of the oxazine ring-opening reaction in the C-trisapm monomer can be analyzed by time-dependent monitoring of the decrease in intensity due to $ArCH_2N$ and $ArCH_2O$ protons by ^{1}H-NMR spectroscopy. Simultaneously, the development of new signals due to the formation of polymer and associated linkages in the PBz network can be monitored. The changes in the magnetic environment of $>CH_2$ in phenolic Mannich, arylamine Mannich, and phenoxy *N*,*O*-acetal linkages is supported by signals in the regions 3.5–4.0, 3.80–4.2 and 4.0–4.4 ppm, respectively.[20,22] Time-dependent normalized ^{1}H-NMR spectra of C-trisapm and its blends with various iron NPs were recorded after heating at 150 °C (Fig. S10†). As compared to blends of NPs with the monomer, neat C-trisapm NMR showed neither changes in the intensity of $ArCH_2N$, $ArCH_2O$ signals nor the appearance of new signals in the range 3.5–4.4 ppm after 7 h, suggesting insignificant polymerization, as it requires a significantly higher curing temperature (T_i = 207 °C). However, the presence of iron NPs in the monomer showed a significant decrease in the $ArCH_2N$ signals with the development of new signals in the region 3.5–4.4 ppm. The upfield signals due to polymer linked in the region 4.4–4.0 ppm are relatively more pronounced than the downfield signals, *i.e.* 4–3.5 ppm, over time. In order to develop a further understanding of the role of iron nanoparticles mediated polymerization, the ^{1}H-NMR spectrum of C-trisapm heated at a higher temperature of 210 °C for 3 h was also recorded and compared to determine the nature of the linkages developed when C-trisapm is treated thermally without NPs. Smaller intensity signals due to its low solubility around 3.8 ppm were noticed, which supports the formation of phenolic Mannich-type structures in polymerization devoid of NPs. In iron NPs treated C-trisapm, $>CH_2$ signals due to phenoxy *N*,*O*-acetal linkages and arylamine Mannich are

still evident while phenolic protons signals due to Mannich-type structures are insignificant (inset of Fig. S10†), which is in agreement with the FTIR analysis (inset of Fig. 4a and S8†). It has previously been reported that double bonds in alkylene chain hydrogens are susceptible to undergoing oxidative crosslinking reactions in cardanol-derived polymers.[49] In our case also, NMR signals due to alkylene chain hydrogens in C-trisapm, in the region 2.4–3.0 ppm, showed noticeable changes, suggesting reaction at these centers. These changes in the NMR signal are more evident in the presence of iron NPs (Fig. S10b–d†). Since the $ArCH_2O$ proton signal was found to be inseparable from the protons due to the alkylene chain and Ar_3CH protons (Fig. S2a†), a time-dependent variation in the intensity of $ArCH_2N$ (with methyl protons as an internal standard) was monitored (Fig. 5b). A decrease in the intensity of $ArCH_2N$ was found to be dependent on the nature of the NPs and it follows the order neat C-trisapm < $(Fe)_0$ < $(Fe)_{TA}$ < $(Fe)_{ATA}$. Amongst NPs, $(Fe)_{ATA}$ contains iron, $-NH_2$ and –COOH functionality and all three are known to assist the ROP in benzoxazine, while $(Fe)_{TA}$ and $(Fe)_0$ possess only two and one curing assistance moieties, thereby lowering their catalytic potential.

Phenols and amines in the presence of iron compounds and peroxidase enzymes tend to undergo oxidative polymerization aided by the iron metal center, with changes in oxidation states +4, +3 or +2.[50] Similarly, benzoxazine monomers are also expected to undergo oxidative polymerization in the presence of a potentially active redox catalyst. Determination of whether a similar mode of polymerization co-exists in an iron NPs blended C-trisapm would enable an understanding of the polymerization mechanism. It was reported previously that the $FeCl_3$-catalyzed reaction of a Bz monomer showed no oxidative linking of monomers in such a fashion.[51] The oxidative reaction of Bz units is expected to proceed in four steps; namely, (i) activation of Bz monomer by electron transfer to the ferric ions in NPs, (ii) which are thereby reduced to ferrous ions, (iii) a coupling reaction of activated Bz monomers, and (iv) regeneration of ferric ions from reduced ferrous ions in NPs. In comparison to the $FeCl_3$ bulk catalyst, the ferrous ions generated in iron NPs tend to re-oxidize at a faster rate due to their higher surface activity with atmospheric air to propagate the coupling reaction of Bz units in a redox manner.[52] Normalized UV-vis analysis of neat C-trisapm monomer before and after heating and in the presence of iron NPs (150 °C for 2 h) was recorded and compared. UV-vis spectra can be divided into two regions, as illustrated in Fig. 5c. A relatively strong absorption at 269 nm and a shoulder at 312 nm are observed for the monomer chromophore, C-trisapm. It is apparent that a relative red-shift of absorption from 269 nm to 276 nm is observed in coated NPs, *i.e.* $(Fe)_{ATA}$ and $(Fe)_{TA}$ (inset in Fig. 5c). While in the presence of $(Fe)_0$, the peak maximum remained at 269 nm, which is the same as for the monomer, but a small red-shifted shoulder developed (inset of Fig. 5c). A new peak centered at ~350 nm with higher intensity is observed in the presence of NPs than in C-trisapm alone when heated under similar conditions. A simultaneous development of absorption maxima in the region 300–400 nm centered at 350 nm suggests the interaction/involvement of Fe NPs in assisting changes in absorption. An increase in the absorption intensity, in particular, beyond the UV region, may be associated with the formation of conjugated aromatic structures as a result of iron NPs mediated polymerization. Previous studies reported that the chemical oxidation of phenol in the presence of peroxidase and oxygen leads to an increase in absorption intensity in the wavelength range of 300–800 nm due to an extension of the degree of polymerization.[53,54] In our case, maxima at short wavelength, around ~260 nm, can be attributed to the localized π–π* transitions whilst at longer wavelengths, ~350 nm, they are accounted for by delocalized π–π* transitions. In general, in conjugated polymers, such as polyphenylenevinylene, a good degree of π-backbone delocalization is observed when the ratio of the intensity of delocalized to localized π–π* transitions is high. For Fe-coated NPs (Table 2), the delocalized π–π* transitions became much stronger than the localized π–π* transitions. Indicating a good level of delocalization along the polymer backbone, which increases with time.

Surprisingly, a low intensity of the delocalized π–π* transitions even in the neat monomer is also observed. The oxidation of benzene to biphenyl and phenol is catalyzed by ferrous ions and hydrogen peroxide, while the formation of the latter is more pronounced in air.[55] Similarly, C-trisapm contains electron-donating oxazine groups like phenol and aniline, along with the presence of Ar_3CH protons, which are prone to an oxidative reaction. However, such a reaction in the monomer may be proceeding at a lower rate compared to when it is blended with iron NPs. In that scenario, bare $(Fe)_0$ NPs are expected to show a higher degree of oxidative polymerization due to more surface exposition of active iron particles and higher concentration of the Fe^{3+} ions (as determined by XRD). In contrast, $(Fe)_0$ showed a lower value of the intensity ratio of delocalized to localized transition than the coated NPs (Table 2). The availability of iron species in NPs was evaluated using a phenanthroline assay, and it was found to be highest in $(Fe)_0$ then $(Fe)_{TA}$, followed by $(Fe)_{ATA}$, (Fig. S11†) confirming our hypothesis. There are nearly 64% and 78% reductions in the availability of iron in $(Fe)_{TA}$ and $(Fe)_{ATA}$, respectively, which are in good agreement with the amount of coating, as determined by TGA analysis (Fig. 3c). In that case, the lower intensity ratio can be accounted for by their oxidative potential, which may not be as favorable as for coated NPs. It was previously reported that the ligands attached to the iron core in complexes control the degree of oxidation by varying the oxidation potential. In an analogy, a coating on NPs may also act like ligands and may be responsible for their higher tendency to form oxidatively polymerized phenyl units in

Table 2 Time-dependent variation in the ratio of intensity of $I_{350\ nm}/I_{269\ nm}$ of C-trisapm heated at 150 °C

	Samples			
Time (h)	C-Trisapm	C-Trisapm $(Fe)_0$	C-Trisapm $(Fe)_{TA}$	C-Trisapm $(Fe)_{ATA}$
2	0.22	0.27	0.42	0.32
5	0.32	0.42	0.66	0.67

a Bz monomer. Furthermore, a higher ratio of the intensity of C-trisapm$(Fe)_{TA}$ to C-trisapm$(Fe)_{ATA}$ is observed after 2 h and the trend in the ratio changed after 5 h (Table 2 and Fig. S12†). A similar trend in data from the UV-vis spectra of $(Fe)_{TA}$ and $(Fe)_{ATA}$ mediated polymerization at 2 h and 5 h is corroborated well by the NMR results (Fig. 5b).

A control reaction was performed to understand the potential of iron NPs in hydrogen peroxide-mediated oxidative polymerization of C-trisapm and the reaction was monitored by UV-vis studies (Fig. 6). The C-trisapm monomer showed an absorption maximum at 258 nm and a shoulder at 304 nm. A lower value in both the λ_{max} and the shoulder in C-trisapm is accounted for by the effect of solvent (Fig. 5c, DMSO *vs.* Fig. 6, THF/water).

Since the monomer was found to be insoluble in DMSO/water, the reaction was performed in THF/water at room temperature. Within 54 h of reaction time at room temperature, a red shift in λ_{max} to 269 nm was observed along with the appearance of a higher intensity maximum at 333 nm. Such changes in UV-vis spectra in the presence of hydrogen peroxide are suggestive of oxidative polymerization, as indicated by an enhancement in the intensity ratio of delocalized to localized π–π^* transitions. However, in the bulk polymerization of the $(Fe)_0$ mediated reaction at 150 °C a similar red shift in localized and delocalized transitions is observed. Furthermore, the intensity of delocalized maxima showed a higher absorbance value, which is accounted for by the utility of higher temperatures, 150 °C *vs.* 28 °C, and may be a result of the instability of the uncoated NPs remaining in a suspension to assist catalysis (see Fig. 1) in solution-based studies. The above results confirm the involvement of NPs in similar modes, as expected in oxidative polymerization in solution.

The reaction mixture of H_2O_2 *vs.* air-mediated polymerization in the presence of $(Fe)_0$ NPs was studied by ^{1}H-NMR spectroscopy. As compared to the monomer, the NMR signals of the formed polymer in general became broad, along with pronounced effects in the aromatic and benzoxazine ring, suggesting reactions at these centers in the presence of iron NPs. In addition, protons due to $ArCH_2N$ and in the region 2.4–3.0 ppm showed significant variation in intensity and appearance (Fig. S13†). No apparent UV-vis changes were observed when the C-trisapm monomer was treated with $(Fe)_0$ NPs alone without the addition of H_2O_2. This suggests that air is playing a role in assisting the above observed UV-vis changes and also at a temperature of 150 °C. The structural changes noticed in ^{1}H-NMR and FTIR along with the changes in UV-vis absorption spectra suggest that several modes of polymerization are active in iron NPs mediated polymerization of a Bz monomer.

The molecular weight of the soluble fraction present in the samples was studied by GPC (Fig. 5d and Table S1†). The observed molecular weight is low, as only the THF-soluble fraction is analyzed. The relative change in M_w and PDI was found to be dependent on the nature of the NPs. A shift to a higher M_w and an increase in its percentage are apparent in the GPC traces, and the incorporation of NPs was found to follow the order neat C-trisapm < $(Fe)_0$ < $(Fe)_{ATA}$ < $(Fe)_{TA}$.

Based on the FTIR, NMR, and UV-vis analysis, and reactive sites available for extending the crosslinked network in PBz, the probable structure of PC-trisapm initiated by iron NPs can be postulated, as in Fig. 7. The coordination of iron or the presence of protons assist the oxazine ring-opening reaction followed by an electrophilic attack of iminium/carbocation to form the polymer network. The major linkage is accounted for by *N*,*O*-acetal, along with phenolic-Mannich, arylamine-Mannich, and biphenyl bridges due to thermal and oxidative polymerization, respectively. The presence of coordinative linkages is also expected due to the coordination of iron with heteroatoms in the PBz framework.

Magnetic properties of NPs and blends

Magnetic properties of different iron NPs and their polymer composites were analyzed (Fig. 8) and are summarized in Table

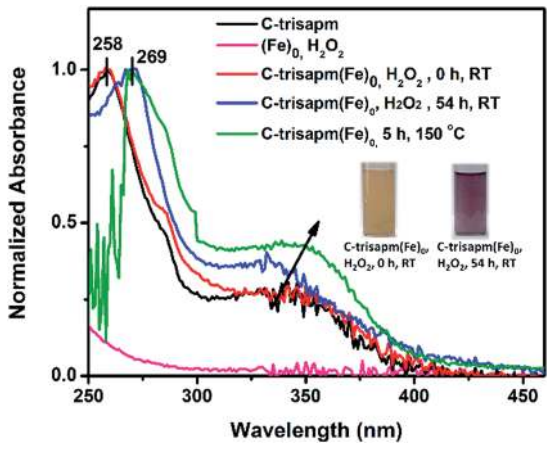

Fig. 6 Probable linkages in the polybenzoxazine network in iron NPs mediated polymerization.

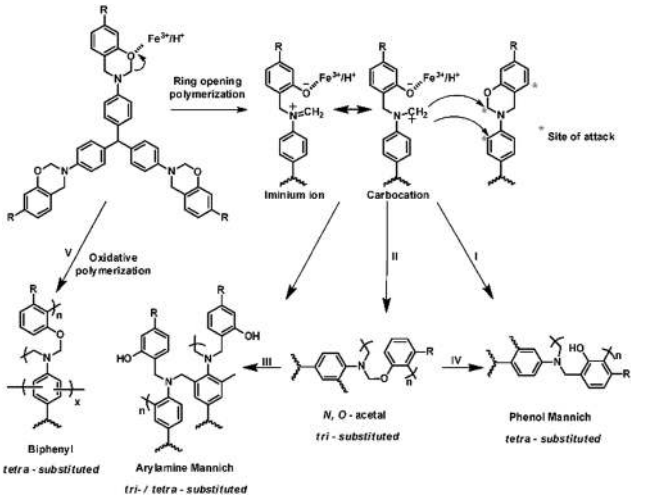

Fig. 7 UV-vis spectra of C-trisapm monomer with $(Fe)_0$ in H_2O_2 and air. Inset shows digital images of a reaction mixture of C-trisapm with $(Fe)_0$ NPs, H_2O_2 at 0 h and 54 h. A characteristic purple colouration is suggestive of an interaction between them affecting the absorption characteristics. However, no colour change is observed when C-trisapm is treated with either $(Fe)_0$ NPs or H_2O_2 alone.

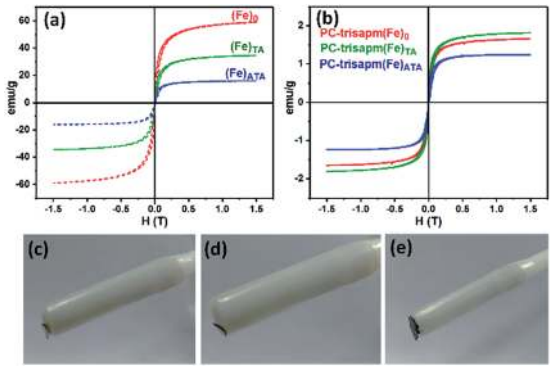

Fig. 8 Magnetic properties at room temperature: hysteresis curve of (a) iron nanoparticles (b) PBz blends with iron NPs, and digital photos of iron NPs containing (c) $(Fe)_0$, (d) $(Fe)_{ATA}$ and (e) $(Fe)_{TA}$ cured PBz resins under a magnetic field.

S2.† The values of the saturation magnetization (M_S), residual magnetism (M_R), and coercivity (H_c) depend on the size, shape, composition, extent and nature of the coating on the NPs. The nanometre size of the NPs as such and in the polymer matrix (as determined by XRD Fig. 2b and 4a), a well-dispersed state (as determined by AFM, Fig. 4c), and zero coercivity indicate the superparamagnetic behavior of the NPs and PBz-nanocomposites. Amongst NPs, the M_S values vary as $(Fe)_{ATA} < (Fe)_{TA} < (Fe)_0$ and the same trend is observed in the case of polymer blends. The value of M_S was found to be highest for bare NPs, at 59 emu g^{-1}, which decreased to 16 emu g^{-1} for coated NPs, which is mainly attributable to the highest degree of coating in $(Fe)_{ATA}$ NPs, agreeing well with our TGA results. The value of M_S can be increased by increasing the loading of NPs in the polymer matrix. However, undesirable agglomeration of the NPs cannot be prevented, with a higher amount of loading affecting other magnetic parameters. The polymer matrix acts as a buffer layer on NPs preventing their degradation and oxidation, thereby minimizing loss of properties or early ageing of the NPs-polymer composite. In polymer composites, a substantial decrease in M_S values of 1.8 emu g^{-1} and 1.2 emu g^{-1} is observed, which is due to lower percentage incorporation (5 wt%) of iron NPs in the matrix and the wrapping of the non-magnetic polybenzoxazine polymer network on the surface of NPs.

Conclusions

This work demonstrates a sustainable approach to the design of polybenzoxazine iron NPs composites using a cost-effective strategy to introduce an agro-waste, cardanol, with different paradigms of properties to advance their applications. The existence of surface functionalities on magnetic iron NPs assisted their dispersion and allowed their uniform distribution into a polymer matrix with retention of their nano-size. The chosen surface functionalities in coated NPs were found to mediate the ROP in Bz, as reflected by a substantial lowering of the curing temperature from 207 °C to 143 °C. Incorporation of only 5 wt% of NPs resulted in a modification of the maximum thermal stability. The interaction of NPs with PBz was extensively analyzed using various spectroscopic techniques to understand the nature of the linkages developed in the polymer. The utilized design strategy of varying the coating in NPs appeared to be an effective one-step smart solution to introducing superparamagnetic behavior along with other benefits. The NPs utilized may find further scope in modifying other polymer-inorganic nanoparticle composites. The superior performances of using low-cost raw materials with facile synthesis is an attractive approach towards promoting renewably sourced cardanol PBz composites at an industrial scale.

Conflicts of interest

There are no conflicts to declare.

Acknowledgements

BL thank the financial support by DST, Ministry of Science & Technology (Grant No. SB/S5/GC-05/2014) and SCCPL, India for providing cardanol. The authors acknowledge financial and infrastructural support from Shiv Nadar Foundation. We also thank the characterization facility provided by AIRF, JNU; NPL, New Delhi and Sprint Testing Solutions, Mumbai.

References

1 H. Ishida and T. Agag, *Handbook of benzoxazine resins*, Elsevier, Amsterdam, 2011, ch. 1, pp. 3–81.
2 N. N. Ghosh, B. Kiskan and Y. Yagci, *Prog. Polym. Sci.*, 2007, **32**, 1344–1391.
3 Global Phenolic Resin Market – By Type, Application, Industry, Regions – Market Size, Demand Forecasts, Industry Trends and Updates, 2016–2022, http://www.researchandmarkets.com, accessed on 2017, Dec 18.
4 US Food and Drug Administration, Bisphenol A (BPA), Use in food contact application, https://www.fda.gov/newsevents/publichealthfocus/ucm064437.htm accessed on 2017, Dec 18.
5 B. Lochab, S. Shukla and I. K. Varma, *RSC Adv.*, 2014, **4**, 21712–21752.
6 A. Parambath, Cashew Nut Shell Liquid, *A goldfield for functional materials*, Springer, 2017, ch. 1, pp. 1–18.
7 B. Lochab, K. Indra and B. Jayashree, *J. Therm. Anal. Calorim.*, 2010, **102**, 769–774.
8 B. Lochab, K. Indra and B. Jayashree, *J. Therm. Anal. Calorim.*, 2012, **107**, 661–668.
9 S. Shukla and B. Lochab, *Green Mater.*, 2017, **5**, 94–102.
10 S. Shukla, M. Tripathi, A. Mahata, B. Pathak and B. Lochab, *Macromol. Chem. Phys.*, 2016, **217**, 1342–1353.
11 T. Endo, *Macromolecules*, 2016, **49**, 8466–8478.
12 B. Lochab, I. K. Varma and J. Bijwe, *J. Therm. Anal. Calorim.*, 2013, **111**, 1357–1364.
13 S. Shukla, A. Ghosh, U. K. Sen, P. K. Roy, S. Mitra and B. Lochab, *ChemistrySelect*, 2016, **1**, 594–600.
14 S. Shukla, A. Ghosh, P. K. Roy, S. Mitra and B. Lochab, *Polymer*, 2016, **99**, 349–357.

15 C. R. Arza, P. Froimowicz and H. Ishida, *RSC Adv.*, 2016, **6**, 35144–35151.
16 H. Y. Low and H. Ishida, *Polymer*, 1999, **40**, 4365–4376.
17 H. Ishida and Y. Rodriguez, *J. Appl. Polym. Sci.*, 1995, **58**, 1751–1760.
18 Y. X. Wang and H. Ishida, *Polymer*, 1999, **40**, 4563–4570.
19 A. Sudo, S. Hirayama and T. Endo, *J. Polym. Sci., Part A: Polym. Chem.*, 2010, **48**, 479–484.
20 C. Liu, D. Shen, R. M. Sebastián, J. Marquet and R. Schönfeld, *Polymer*, 2013, **54**, 2873–2878.
21 C. Liu, D. Shen, R. M. Sebastián, J. Marquet and R. Schönfeld, *Macromolecules*, 2011, **44**, 4616–4622.
22 Q. C. Ran, D. X. Zhang, R. Q. Zhu and Y. Gu, *Polymer*, 2012, **53**, 4119–4127.
23 P. Sharma, M. Srivastava, B. Lochab, D. Kumar, A. Ramanan and P. K. Roy, *ChemistrySelect*, 2016, **1**, 3924–3932.
24 T. Gelbrich, M. Feyen and A. M. Schmidt, *Macromolecules*, 2006, **39**, 3469–3472.
25 K. R. Reddy, W. Park, B. C. Sin, J. Noh and Y. Lee, *J. Colloid Interface Sci.*, 2009, **335**, 34–39.
26 S. Shukla, A. Mahata, B. Pathak and B. Lochab, *RSC Adv.*, 2015, **5**, 78071–78080.
27 D. Maity, G. Zoppellaro, V. Sedenkova, J. Tucek, K. Safarova, K. Polakova, K. Tomankova, C. Diwoky, R. Stollberger and L. Machala, *Chem. Commun.*, 2012, **48**, 11398–11400.
28 D. Wang, J. Zhou, R. Chen, R. Shi, G. Xia, S. Zhou, Z. Liu, N. Zhang, H. Wang and Z. Guo, *Biomaterials*, 2016, **107**, 88–101.
29 A. H. Lu, E. e. L. Salabas and F. Schüth, *Angew. Chem., Int. Ed.*, 2007, **46**, 1222–1244.
30 W. Lu, Y. Shen, A. Xie and W. Zhang, *J. Magn. Magn. Mater.*, 2010, **322**, 1828–1833.
31 C. Cui, Y. Du, T. Li, X. Zheng, X. Wang, X. Han and P. Xu, *J. Phys. Chem. B*, 2012, **116**, 9523–9531.
32 T. Phenrat, Y. Liu, R. D. Tilton and G. V. Lowry, *Environ. Sci. Technol.*, 2009, **43**, 1507–1514.
33 G. Christensen, H. Younes, H. Hong and P. Smith, *J. Appl. Phys.*, 2015, **118**, 214302.
34 B. l. Kharisov, H. V. R. Dias, O. V. Kharissova, A. Vazquez, Y. Peña and I. Gómez, *RSC Adv.*, 2014, **4**, 45354–45381.
35 Dynamic viscosity of tetrahydrofuran and chloroform, Dortmund data bank, http://www.ddbst.com, accessed on 2017, Dec 22.
36 N. Sini, J. Bijwe and I. K. Varma, *J. Polym. Sci., Part A: Polym. Chem.*, 2014, **52**, 7–11.
37 B. Kiskan, A. L. Demirel, O. Kamer and Y. Yagci, *J. Polym. Sci., Part A: Polym. Chem.*, 2008, **46**, 6780–6788.
38 J. Sun, W. Wei, Y. Xu, J. Qu, X. Liu and T. Endo, *RSC Adv.*, 2015, **5**, 19048–19057.
39 R. Andreu, J. A. Reina and J. C. Ronda, *J. Polym. Sci., Part A: Polym. Chem.*, 2008, **46**, 6091–6101.
40 S. Shukla and B. Lochab, *Polymer*, 2016, **99**, 684–694.
41 H. Y. Low and H. Ishida, *Polym. Degrad. Stab.*, 2006, **91**, 805–815.
42 Y. X. Wang and H. Ishida, *Macromolecules*, 2000, **33**, 2839–2847.
43 A. Sudo, R. Kudoh, H. Nakayama, K. Arima and T. Endo, *Macromolecules*, 2008, **41**, 9030–9034.
44 H. Y. Low and H. Ishida, *J. Polym. Sci., Part B: Polym. Phys. Ed.*, 1998, **36**, 1935–1946.
45 L. Han, D. Iguchi, P. Gil, T. R. Heyl, V. M. Sedwick, C. R. Arza, S. Ohashi, D. J. Lacks and H. Ishida, *J. Phys. Chem. A*, 2017, **121**, 6269–6282.
46 A. S. Jadhav, R. Bongiovanni, L. D. Marchisio, D. Fontana and C. Egger, *Pigm. Resin Technol.*, 2014, **43**, 219–227.
47 J. F. Rabek, J. Lucki, B. Qu and W. Shi, *Macromolecules*, 1991, **24**, 836–843.
48 P. Thirukumaran, A. S. Parveen and M. Sarojadevi, *Polym. Compos.*, 2015, **36**, 1973–1982.
49 S. Manjula, V. Kumar and C. Pillai, *J. Appl. Polym. Sci.*, 1992, **45**, 309–315.
50 I. Yamazaki and K. Yokota, *Mol. Cell. Biochem.*, 1973, **2**, 39–52.
51 B. Kiskan, Y. Yagci, E. Sahmetlioglu and L. Toppare, *J. Polym. Sci., Part A: Polym. Chem.*, 2007, **45**, 999–1006.
52 V. Bhanu and K. Kishore, *Chem. Rev.*, 1991, **91**, 99–117.
53 P. K. Jha and G. P. Halada, *Chem. Cent. J.*, 2011, **5**, 12.
54 F. F. Bruno, R. Nagarajan, P. Stenhouse, K. Yang, J. Kumar, S. K. Tripathy and L. A. Samuelson, *J. Macromol. Sci., Part A: Pure Appl. Chem.*, 2001, **38**, 1417–1426.
55 J. Baxendale and J. Magee, *Discuss. Faraday Soc.*, 1953, **14**, 160–169.